Available online at www.sciencedirect.com
ScienceDirect
Journal of Colloid and Interface Science 308 (2007) 231–238
JOURNAL OF Colloid and Interface Science
www.elsevier.com/locate/jcis

Transport of wetting liquid plugs in bifurcating microfluidic channels

Cédric P. Ody, Charles N. Baroud *, Emmanuel de Langre

Laboratoire d'Hydrodynamique (LadHyX), Ecole Polytechnique-CNRS, 91128 Palaiseau Cedex, France

Received 16 August 2006; accepted 5 December 2006

Available online 12 December 2006

Abstract

A plug of wetting liquid is driven at constant pressure through a bifurcation in a microchannel. For a plug advancing in a straight channel, we find that the viscous dissipation in the bulk may be estimated using Poiseuille's law while Bretherton and Tanner's laws model the additional dissipation occurring at the rear and front interfaces. At a second stage, we focus on the behavior of the plug flowing through a T-junction. Experiments show the existence of a threshold pressure, below which the plug remains blocked at the entrance of the junction. Above this required pressure, the plug enters the bifurcation and either ruptures or splits into two daughter plugs, depending on the applied pressure and on the initial length of the plug. By means of geometrical arguments and the previously cited laws, we propose a global model to predict the transitions between the three observed behaviors.

Keywords: Microfluidic bifurcation; Plug rupture; Threshold pressure; Splitting

1. Introduction

Microfluidic fabrication techniques provide new ways to handle fluids in complex geometries at sub-millimeter scale. While the transport of a single fluid is well understood in the laminar "Stokes" regime, two-phase flows present important challenges due to the nonlinear effects at the moving interfaces. Indeed, even the transport of liquid plugs in a straight channel involves a nonlinear pressure–velocity relationship that results from the balance between viscous and capillary effects [1]. This balance operates near the triple lines at which the liquid and gas phases meet the solid substrate; the details of this balance depend strongly on the wetting properties of the solid and the liquid [2].

The transport of plugs in a complex geometry, such as a network of channels, is of interest for microfluidics but also in geological and biological situations. For instance, an understanding of the transport of plugs through bifurcations is necessary for applications in drug delivery in the pulmonary airway tree [3], or in the extraction of oil from porous rocks [4], where one is interested in the transport of a volume of a liquid (mucus or petroleum) bounded by two liquid–gas interfaces. Since the liquid usually wets the solid in these situations, this will be represented at rest by a zero contact angle between the two phases.

The aim of the present work is to study the transport of such plugs in rectangular microchannels, when both inertia and gravity are negligible. This is done by driving plugs at constant pressure through straight and bifurcating microchannels and by developing corresponding theoretical models. A combined theoretical and experimental study of the straight and bifurcating cases will therefore provide the essential building block for understanding the dynamics of a two-phase flow in a channel network, which in turn will allow the modeling of concrete situations.

The paper is structured as follows: Section 2 presents the experimental setup and protocol. It is followed in Section 3 by the development of a theoretical model for a plug in a straight channel which is validated experimentally. Finally, Sections 4 and 5 provide the experimental and theoretical study of the flow of a plug through a T-junction, respectively.

* Corresponding author.
E-mail address: baroud@ladhyx.polytechnique.fr (C.N. Baroud).

0021-9797/$ – see front matter
doi:10.1016/j.jcis.2006.12.018

2. Experimental setup

A schematic of the experimental setup used in our study is shown in Fig. 1. The experiments were conducted in rectangular cross section microfluidic channels made of polydimethylsiloxane (PDMS) by using soft lithography techniques [5]. These channels are integrated in a microfluidic chip, composed of two parts. To obtain the upper part in which the channel is etched, a thin layer of photosensitive resin (Microchem, SU8-2035) is first spin-coated on a silicon wafer and patterned by standard photolithography. The speed of spin-coating sets the thickness b of the future channels, while the widths and the shapes are controlled by the design of the patterned masks which are used during the UV exposure. The photoresist is then developed yielding the mold on which a thick layer of PDMS (Dow Corming, Sylgard 184) is poured and allowed to partially cure. The resulting cast is finally removed from the mold and inlet/outlet holes are punched for later connections. In parallel, the lower part of the microchannel is obtained by spin-coating and partially curing a flat layer of PDMS on a glass microscope slide. At a final stage, the two PDMS parts are brought into contact and the whole is cured completely, thus forming a microfluidic chip. As seen in Fig. 1, the microchannel consists of an entrance region (Y-junction) used to form the liquid plugs, an initial straight channel and a final T-junction. We note that w_i and w_o are the widths of the inlet and outlet branches of the T-junction. Typical values for the thickness and the width of the straight channel were $b \simeq 25$–50 μm and $w_\mathrm{i} \simeq 200$–300 μm. The different dimensions were measured on the resin mold with a profilometer (Dektak).

A constant driving pressure P_dr was applied using a water column connected to a sealed air bottle as shown in Fig. 1; the air flowing out of the bottle was then driven to one inlet of the Y-junction while the other inlet was used for liquid introduction. Outlets of the T-junction were at atmospheric pressure P_0. Different values of the driving pressure P_dr were obtained by varying the height of water in the column and calculating the corresponding hydrostatic pressure, ranging from 100 Pa (≃1 cm of water) up to 600 Pa (≃60 cm of water). The precision on the water height pressure was 2 mm, giving a maximum error of 20% for the lowest pressure value. All pressure losses in the external tubing were neglected.

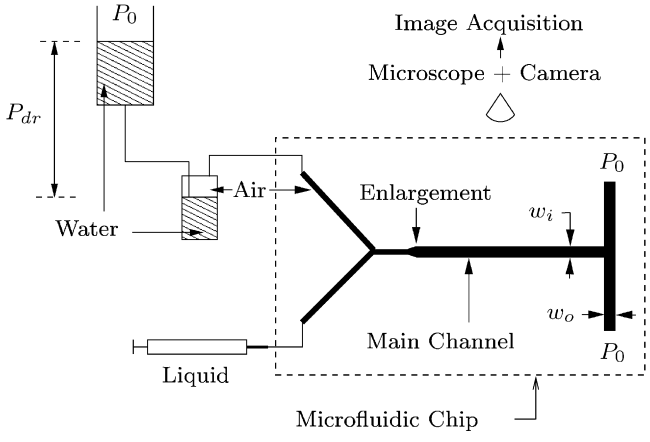

Fig. 1. Experimental setup. A constant pressure P_dr is applied at the upper left inlet branch of the Y-junction. The lower left branch is used to introduce the wetting liquid from a syringe pump. The motion of the plug is recorded with a camera through a microscope. Note the enlargement of the inlet channel downstream of the Y-junction.

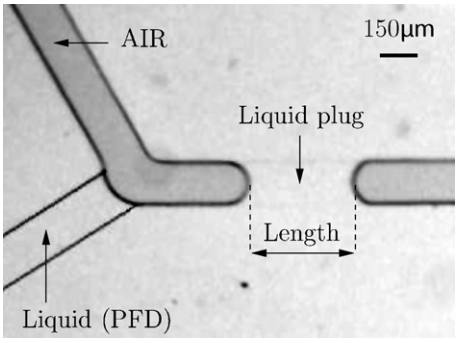

Fig. 2. A liquid plug after its formation within the Y-junction. The plug moves from left to right. The upper branch is connected to the constant pressure source (air) and the lower branch contains the wetting liquid which is injected using a syringe pump. Length and speed are calculated from the measured positions of the menisci at the advancing (front) and receding (rear) interfaces, detected along the centerline of the channel.

The plugs were formed with perfluorodecalin (PFD), a fluorinated liquid with dynamic viscosity $\eta = 5$ cP and surface tension $\gamma = 15$ mN/m [6]. In addition to wetting the solid substrate, the PFD also has the advantage of not swelling the PDMS [7]. To obtain the typical plug shown in Fig. 2, the liquid was forced into one inlet of the Y-junction by actuating a syringe pump for a given interval of time while a manual valve cut off the air entrance from the pressure source. Once the plug was formed, the syringe pump was switched off, and the pressure was applied. By controlling the duration of the syringe pump actuation, plugs of different lengths were obtained. However, since the minimal length of the plugs was fixed by the characteristic size of the Y-junction, the channel was enlarged downstream of the Y-junction to allow the study of shorter plugs, resulting in lengths as small as the width w_i of the inlet channel. There was no upper limit for the size of the plugs.

Experiments were recorded with a high speed camera (resolution 1024×256 pixels, 1 pixel for 10 μm, sampled at 10–100 fps) through a microscope (Leica, MZ 16). For each image of the sequences thus obtained, the positions (x_f and x_r) of the menisci at the advancing (front) and receding (rear) interfaces of the traveling plug were manually located along the centerline of the channel. These measurements yielded the length and the speed of the plug during its transport as, respectively, $L_\mathrm{plug} = x_\mathrm{f} - x_\mathrm{r}$ and $U_\mathrm{plug} = \mathrm{d}x_\mathrm{c}/\mathrm{d}t$ with $x_\mathrm{c} = (x_\mathrm{f} + x_\mathrm{r})/2$. Note that before starting data acquisition, several plugs of PFD were introduced in order to prewet the channel walls.

A sketch of a plug moving in a rectangular microchannel is shown in Fig. 3. In this schematic, plane A ("in-plane" section) represents the projected view as seen through the microscope, e.g., Fig. 2. We will also refer later to plane B as the "in-thickness" section.

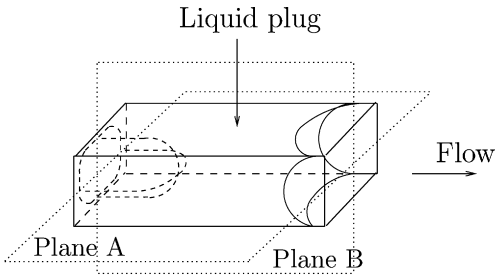

Fig. 3. Schematic of a plug in a rectangular channel. Planes A and B correspond respectively to "in-plane" and "in-thickness" sections.

3. Visco-capillary regime in straight channels

We first consider the transport of a liquid plug of length L_0 moving with a steady velocity U_0 in the straight microchannel upstream of the T-junction. By taking a characteristic length scale $D \sim 50$ μm and typical velocities $U_0 \sim 5$ mm/s, one obtains a Bond number $\mathrm{Bo} = \rho g D^2/\gamma \sim 5\times 10^{-3}$ and a Reynolds number $\mathrm{Re} = \rho U_0 D/\eta \sim 2\times 10^{-2}$, where $\rho \sim 1000$ kg/m^3 and $g = 9.81$ m/s^2 are, respectively, the density of the liquid and the acceleration of gravity. Therefore, one may neglect gravity and inertial effects, expecting the plug dynamics to be governed by a visco-capillary regime as mentioned in [8]. Here, we use an approach similar to the one developed by Bico and Quéré [1]. Given a constant driving pressure P_{dr}, the steady-state pressure balance across the plug is

$$P_{\mathrm{dr}} = \Delta P^{\mathrm{r}}_{\mathrm{cap}} + P_{\mathrm{visc}} + \Delta P^{\mathrm{a}}_{\mathrm{cap}}, \tag{1}$$

where $\Delta P^{\mathrm{r}}_{\mathrm{cap}}$ and $\Delta P^{\mathrm{a}}_{\mathrm{cap}}$ express the capillary pressure drops at the receding and advancing interfaces of the plug, respectively, while P_{visc} represents the viscous dissipation occurring in the bulk. Using Poiseuille's law, the latter is expressed as

$$P_{\mathrm{visc}} = \alpha\eta L_0 U_0, \tag{2}$$

with α, a dimensional coefficient, corresponding to the geometry of the channel. For a rectangular geometry [9], α may be approximated as

$$\alpha \simeq \frac{12}{b^2}\left[1 - 6\frac{2^5 b}{\pi^5 w_{\mathrm{i}}}\right]^{-1}. \tag{3}$$

When the plug is at rest, static values of $\Delta P^{\mathrm{r}}_{\mathrm{cap}}$ and $\Delta P^{\mathrm{a}}_{\mathrm{cap}}$ are given by Laplace's law as $\Delta P^{\mathrm{r}}_{\mathrm{cap}} = -\Delta P^{\mathrm{a}}_{\mathrm{cap}} = \gamma\kappa$, where $\kappa \simeq 2(b^{-1} + w_{\mathrm{i}}^{-1})$ is the mean curvature of each interface at rest. Here, we neglect the flow of liquid along the corners of the channel that slightly deforms the shape of the interfaces [10]. When the plug is moving, the front and rear curvatures are modified as shown in Fig. 4. At the front interface, the balance between friction and wetting forces at the vicinity of the contact line leads to the existence of a non-zero dynamic contact angle and this flattening of the advancing interface increases the resistance to the motion. By assuming that θ^{a} has the same value in the two sections, the dynamic capillary pressure drop for the front interface becomes

$$\Delta P^{\mathrm{a}}_{\mathrm{cap}} = -\gamma\kappa\cos\theta^{\mathrm{a}}. \tag{4}$$

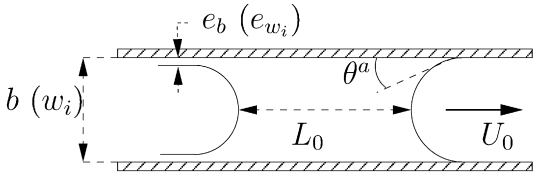

Fig. 4. Sketch of the plug (sections A and B). Here, θ^{a} is the dynamic contact angle at the front interface and e_{b} ($e_{w_{\mathrm{i}}}$) is the thickness of the deposited film at the rear of the plug in the thickness (width).

The relation between the contact angle and the velocity of the contact line is known through Tanner's law [1,11] which states that

$$\theta^{\mathrm{a}} = (6\Gamma\mathrm{Ca})^{1/3}, \tag{5}$$

where $\mathrm{Ca} = \eta U_0/\gamma$ is the capillary number and Γ is a logarithmic prefactor that accounts for the singularity occurring at the contact line, where the usual no-slip boundary condition at the solid surface leads to a logarithmic divergence in the shear stress [12].

Using Eq. (5) and taking the first-order term in the Taylor expansion of $\cos\theta^{\mathrm{a}}$ in Eq. (4), the front pressure drop becomes

$$\Delta P^{\mathrm{a}}_{\mathrm{cap}} \simeq \gamma\kappa\left(-1 + \frac{(6\Gamma\mathrm{Ca})^{2/3}}{2}\right). \tag{6}$$

At the rear interface, a thin film is deposited at the channel walls [13], which reduces the rear meniscus radius and thus, also increases the resistance to the motion. We note that e_{b} and $e_{w_{\mathrm{i}}}$ are the thicknesses of the deposited film at the rear of the plug in the in-thickness and in-plane sections, respectively. The dynamic capillary pressure drop at the rear interface may then be written as

$$\Delta P^{\mathrm{r}}_{\mathrm{cap}} = \gamma\left(\frac{1}{b/2 - e_{\mathrm{b}}} + \frac{1}{w_{\mathrm{i}}/2 - e_{w_{\mathrm{i}}}}\right). \tag{7}$$

Bretherton's law expresses the thickness e of the deposited film at the rear of a plug as a function of the capillary number Ca and the radius R of a circular capillary tube [1]:

$$e/R = 3.88\mathrm{Ca}^{2/3}. \tag{8}$$

Assuming Bretherton's law to be valid in both directions of the rectangular cross section, i.e., $2e_{\mathrm{b}}/b = 2e_{w_{\mathrm{i}}}/w_{\mathrm{i}} = 3.88\mathrm{Ca}^{2/3}$, the rear capillary jump is obtained from Eq. (7) as

$$\Delta P^{\mathrm{r}}_{\mathrm{cap}} = \gamma\kappa\left(1 + 3.88\mathrm{Ca}^{2/3}\right). \tag{9}$$

Finally, by using Eqs. (2), (6) and (9), one derives

$$P_{\mathrm{dr}} \simeq \alpha\eta L_0 U_0 + \gamma\kappa\beta\mathrm{Ca}^{2/3}, \tag{10}$$

where $\beta = 3.88 + (6\Gamma)^{2/3}/2$ is a nondimensional coefficient obtained from Bretherton's and Tanner's laws.

Equation (10) governs the dynamics of a plug of length L_0 moving steadily at speed U_0 in a straight rectangular channel for a constant driving pressure. Equation (10) can be nondimensionalized by comparing it with the capillary pressure jump $\gamma\kappa$, and we obtain

$$\overline{P_{\mathrm{dr}}} \simeq \bar{\alpha}\mathrm{Ca} + \beta\mathrm{Ca}^{2/3}, \tag{11}$$

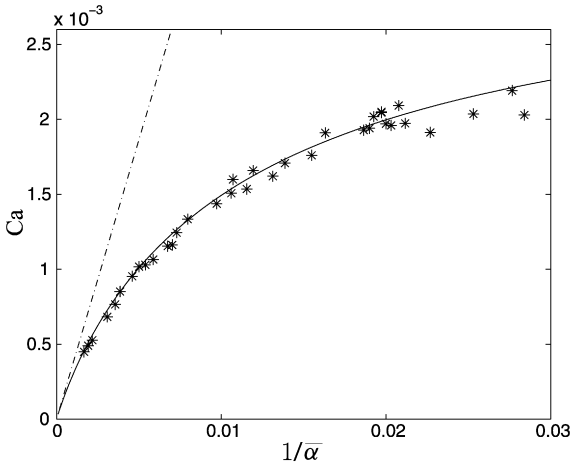

Fig. 5. Capillary number of a liquid plug as a function of its inverse nondimensional length $1/\bar{\alpha}$ for a pressure $P_{\mathrm{dr}} = 250$ Pa ($\overline{P_{\mathrm{dr}}} = 0.2$). The dashed line corresponds to Poiseuille's law, $\mathrm{Ca} \propto 1/\bar{\alpha}$. The full line corresponds to Eq. (11) with $\beta = 16$.

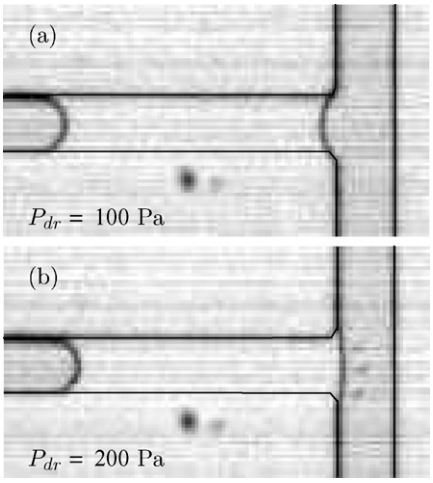

Fig. 6. Blocking of the plug at the entrance of the T-junction for two distinct pressures with $P_{\mathrm{dr}} < P_{\mathrm{thresh}}$. The front interface is pinned at the corners of the bifurcation and adapts its curvature to the applied pressure. The shape of the rear interface is independent of P_{dr}.

with $\overline{P_{\mathrm{dr}}} = P_{\mathrm{dr}}/(\gamma\kappa)$ is the nondimensional driving pressure and $\bar{\alpha} = \alpha L_0/\kappa$ is the nondimensional length.

Experiments were conducted in a microchannel to verify the applicability of Eq. (11) to our rectangular geometry. The cross section of the microchannels used here was $w_{\mathrm{i}} \times b = 210 \times 25$ μm. Single plugs of various lengths were introduced and forced at constant pressure following the protocol of Section 2. For all driving pressures, we observed that the measured lengths and speeds of the plugs remained constant within 5% throughout the channel and average length L_0 and speed U_0 were determined.

A sample of experimental results is plotted in Fig. 5. Data corresponding to long plugs asymptote to Poiseuille's law (dashed line, $\overline{P_{\mathrm{dr}}} = \bar{\alpha}\mathrm{Ca}$ from Eq. (2)). For shorter plugs, the data exhibit a nonlinear Ca vs $(\bar{\alpha})^{-1}$ relationship due to an additional dissipation occurring at the interfaces. The theoretical curve (full line) obtained from Eq. (11) is plotted with $\beta = 16$ and is in good agreement with the experimental data. The corresponding value of $\Gamma = 20$ is higher than experimental values reported in millimetric circular tubes [1]. However, the coefficient $(6\Gamma)^{1/3} = 4.9$ appearing in Tanner's law (Eq. (5)) is in close agreement with Hoffman's data [11] for which the previous coefficient is of order 4–5 for a dry tube. A more precise estimate of the Tanner's constant would require a specific study by keeping track of both the microscopic and macroscopic physics involved in our configuration, as described in [12].

Thus, although Bretherton's and Tanner's laws are not strictly applicable to the rectangular geometry, our results show the possibility of using the previous laws to model the dynamics of plugs in our channels.

4. Blocking, rupture or splitting at the T-junction

We now consider a plug flowing through the T-junction for different driving pressures and initial plug lengths, L_0, measured in the straight channel upstream of the bifurcation. Experiments were conducted with channel dimensions $w_{\mathrm{i}} \times w_{\mathrm{o}} \times b = 260 \times 260 \times 46$ μm. Three different behaviors were observed depending on the driving pressure and on the initial length of the plug as described below.

4.1. Blocking

The first feature extracted from the observations of a plug getting to the T-junction is the existence of a threshold pressure P_{thresh} (between 200 and 300 Pa for our experiments) which does not depend on the initial length of the plug. For $P_{\mathrm{dr}} < P_{\mathrm{thresh}}$, the plug remains blocked at the entrance of the bifurcation as presented in Fig. 6, which shows the equilibrium positions of plugs for two distinct pressures ($P_{\mathrm{dr}} = 100$, 200 Pa). While the rear interface has the same shape in both cases, the front interface adapts its curvature to balance the applied pressure keeping its extremities pinned at the corners of the bifurcation.

4.2. Rupture

When the pressure exceeds the threshold pressure P_{thresh}, the plug continues its propagation through the bifurcation. If the plug is short, its rear interface catches up with its front interface before the latter reaches the wall opposite to the entrance channel. The plug then ruptures, opening the outlet branches of the T-junction to air. A typical sequence of plug rupture is shown in Fig. 7. Eventually, the liquid that remains on the channel walls drains slowly through the action of capillary forces and air drag.

4.3. Splitting into two daughter plugs

When the plugs are sufficiently long that the front interface reaches the opposite wall, two daughter plugs of equal length are formed through a splitting of the initial one, as shown in Fig. 8. As soon as the liquid reaches the wall, the transport

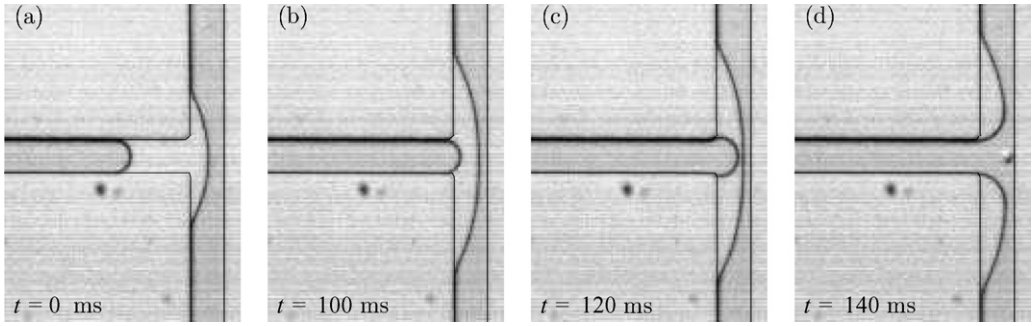

Fig. 7. Sequence of plug rupture. The plug ruptures in the T-junction, leaving liquid on one side of the outlet channel, where air can flow freely from the pressure source.

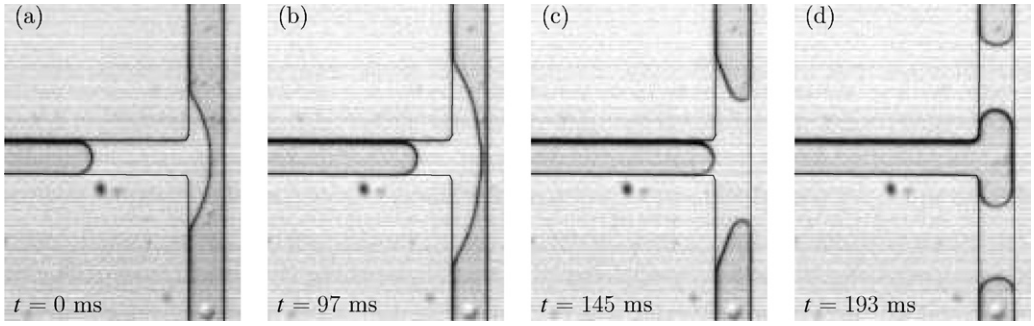

Fig. 8. Sequence of plug splitting at the T-junction. Splitting leads to symmetric formation of two daughter plugs in the outlet branches of the T-junction.

dynamics becomes dominated by the wetting forces acting between the two phases. These forces act to draw the liquid very rapidly into contact with the wall, as observed between the images (b) and (c) of Fig. 8. In part (c), we see that the curvature is not constant along the liquid surface, implying local pressure gradients in the fluid which pull it into the daughter branches. These wetting forces are dominant compared to the driving pressure, as seen by the rapidity of the advance once the plug has touched the wall.

Note that before rupture or splitting, the evolution of the plug in the bifurcation is similar in both cases: the front interface advances without constraints while the extremities of the rear interface remain pinned by the corners of the bifurcation until process of rupture or splitting is achieved (Fig. 7c).

4.4. Phase diagram

We summarize the three cases discussed above (blocking, rupture and splitting) in the experimental phase diagram shown in Fig. 9. As stated above, we observed the blocking (△) of the plug below a threshold pressure, P_{thresh}, whose value is seen to be independent on the length of the plug. Above P_{thresh}, experimental data show that the transition between rupture (■) and splitting (○) depends on the applied pressure and on the length of the plug: as the pressure increases, the length of liquid required to create two daughter plugs becomes smaller.

5. Theoretical model

In this section, the two transitions appearing in the phase diagram of Fig. 9 are explained theoretically. We first establish a

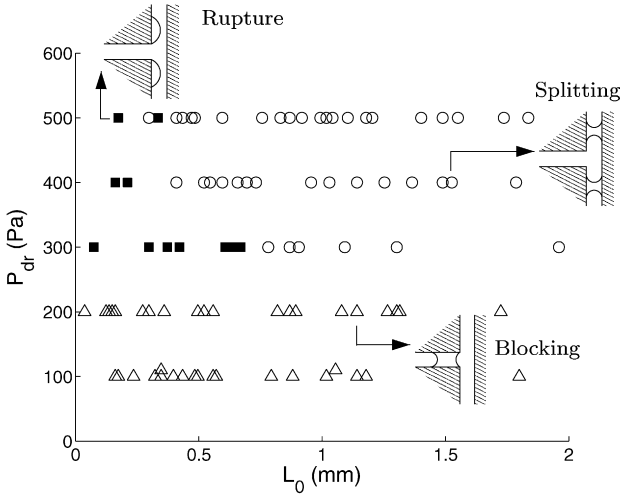

Fig. 9. Phase diagram for plug behavior at the T-junction.

2D pressure balance to derive the value of the blocking pressure after which we develop a model to predict the transition between rupture and splitting.

5.1. Threshold pressure

Since the plug is at rest in the blocking case, the viscous term in Eq. (1) is zero and the new pressure balance may be written as

$$P_{\text{dr}} = \Delta P^{\text{r}}_{\text{cap}} + \Delta P^{\text{a}}_{\text{cap}}. \tag{12}$$

Here, the terms $\Delta P^{\text{r}}_{\text{cap}}$ and $\Delta P^{\text{a}}_{\text{cap}}$ express static pressure drops and Eq. (12) may be simplified by distinguishing in-plane and

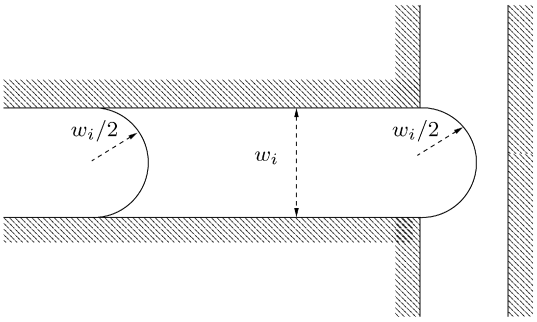

Fig. 10. The shapes of the rear and front interfaces at the threshold pressure (in-plane section).

in-thickness contributions of the capillary pressure jumps which are related via Laplace's law to the corresponding principal curvatures of the interfaces. Since the channel thickness does not vary at the bifurcation, we assume that the in-thickness components of the pressure drops at the rear and front interfaces cancel each other, the radii of curvature in the thickness being $b/2$ in absolute value. Therefore, the problem is reduced to a 2D pressure balance of in-plane components of pressure drops, leading to

$$P_{\mathrm{dr}} = \gamma\left(\frac{1}{R^{\mathrm{r}}} + \frac{1}{R^{\mathrm{a}}}\right), \tag{13}$$

where R^{r} and R^{a} are the radii of curvature of the rear and front interfaces in plane A, respectively.

The experimental observations shown in Fig. 6 provide the information to derive the value of the threshold pressure. For $P_{\mathrm{dr}} < P_{\mathrm{thresh}}$, the receding interface is seen to keep a constant in-plane radius of curvature $R^{\mathrm{r}} = w_{\mathrm{i}}/2$ while the advancing interface adapts its in-plane curvature to the applied pressure and its radius R^{a} varies such that $|R^{\mathrm{a}}| \geqslant w_{\mathrm{i}}/2$. The situation in which $R^{\mathrm{a}} = +w_{\mathrm{i}}/2$ is illustrated in Fig. 10 and leads to the threshold pressure, which is the highest pressure that can be sustained across the plug, reading finally

$$P_{\mathrm{thresh}} = \frac{4\gamma}{w_{\mathrm{i}}}. \tag{14}$$

For our experimental conditions ($w_{\mathrm{i}} = 260\,\mu\mathrm{m}$ and $\gamma = 15\,\mathrm{mN/m}$), we obtain $P_{\mathrm{thresh}} \simeq 230\,\mathrm{Pa}$, in agreement with the measured value ($200\,\mathrm{Pa} < P_{\mathrm{thresh}} < 300\,\mathrm{Pa}$).

5.2. Rupture or splitting

We now propose to explain the critical plug length, L_{crit}, for getting rupture or splitting when the pressure exceeds the threshold pressure. Our aim here is not to model the complete dynamics of the plug but to derive a global model which clarifies the dependence of L_{crit} on the driving pressure P_{dr} by taking into account the fundamental mechanisms involved in the plug evolution. We first consider a plug of length L_{crit} theoretically situated on the transition curve. A geometric condition is then obtained from the shape of such a plug in the T-junction. Finally, a dynamic argument is used to map this geometric condition onto the experimental L_0–P_{dr} diagram.

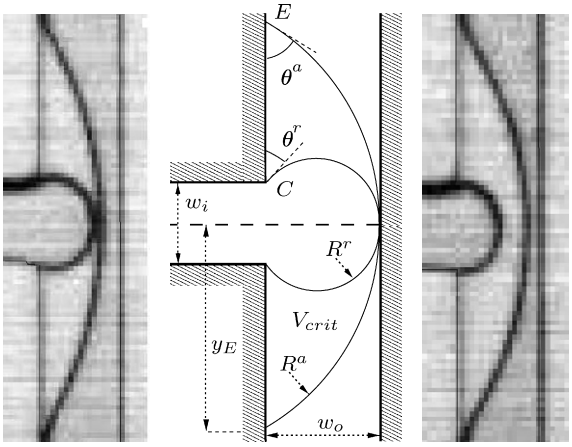

Fig. 11. Shape of the plugs before (a) rupture and (c) splitting. (b) Schematic of a plug of volume V_{crit} situated on the theoretical boundary between rupture and splitting where front and rear interfaces of a plug meet at the wall.

5.2.1. Geometric condition

The diagram of Fig. 9 exhibits a L_0–P_{dr} dependent boundary between the rupture or splitting cases. We consider the shape of the plugs just before rupture or splitting, as shown in Figs. 11a and 11c. In Fig. 11a, the rear interface catches up with the front interface before the latter reaches the wall, leading to rupture of the plug. Conversely, in Fig. 11c, the front interface is about to touch the wall before the rear interface catches up with it, resulting in the splitting of the plug and the formation of two daughter plugs. In the limiting case, a plug of length L_{crit} sees its front and rear interfaces meeting at the wall. Approximating the shape of both interfaces with circular sections leads to the sketch of Fig. 11b. Here, the critical volume of the plug is noted V_{crit} and is completely defined by θ^{a}, θ^{r}, w_{o} and the thickness b of the microchannel. At point C, the rear contact angle θ^{r} is defined geometrically as $\theta^{\mathrm{r}} = 2\arctan(w_{\mathrm{i}}/2w_{\mathrm{o}})$. In contrast, the contact angle θ^{a} at point E may take different values depending on the velocity of the advancing interface. As a result, the critical volume decreases as θ^{a} increases for a given T-junction, down to a zero volume when $\theta^{\mathrm{a}} = \pi - \theta^{\mathrm{r}}$.

The volume of liquid contained between the two interfaces in the critical configuration corresponding to Fig. 11b is obtained as

$$V_{\mathrm{crit}} = b w_{\mathrm{o}}^2\big[f\big(\theta^{\mathrm{a}}\big) - g\big(\theta^{\mathrm{r}}\big)\big], \tag{15}$$

where

$$f\big(\theta^{\mathrm{a}}\big) = \big(\theta^{\mathrm{a}} - \cos\theta^{\mathrm{a}}\sin\theta^{\mathrm{a}}\big)\big(1 - \cos\theta^{\mathrm{a}}\big)^{-2} \tag{16}$$

and

$$g\big(\theta^{\mathrm{r}}\big) = \big(\pi - \theta^{\mathrm{r}} + \cos\theta^{\mathrm{r}}\sin\theta^{\mathrm{r}}\big)\big(1 + \cos\theta^{\mathrm{r}}\big)^{-2}. \tag{17}$$

This volume corresponds to a plug of length L_{crit} in the entrance channel such that

$$V_{\mathrm{crit}} = b\big[L_{\mathrm{crit}} w_{\mathrm{i}} + (1 - \pi/4) w_{\mathrm{i}}^2\big], \tag{18}$$

with the correction term $b(1 - \pi/4)w_{\mathrm{i}}^2$ taking into account the volume contained in the circular menisci. Therefore, the critical

length is such that

$$\frac{L_{\text{crit}}}{w_{\text{i}}} = \left(\frac{w_{\text{o}}}{w_{\text{i}}}\right)^2 \left[f\left(\theta^{\text{a}}\right) - g\left(\theta^{\text{r}}\right)\right] - \left(1 - \frac{\pi}{4}\right). \tag{19}$$

For a given contact angle θ^{a}, a plug of initial length $L_0 < L_{\text{crit}}$ will rupture in the bifurcation while a plug such that $L_0 > L_{\text{crit}}$ will produce two daughter plugs.

Since θ^{r} is a function of the ratio $w_{\text{o}}/w_{\text{i}}$, the value of L_{crit} depends on θ^{a} and $w_{\text{o}}/w_{\text{i}}$. Therefore, Eq. (19) will provide different values of L_{crit} as θ^{a} varies, the other quantities being constant for a given geometry. The problem is now to understand the mechanisms involved in the determination of θ^{a}.

5.2.2. Dynamic condition

Although the propagation in the bifurcation is unsteady, the dynamics is still governed by a visco-capillary regime. Therefore, at a given time, we may use Eq. (1) on a specific fluid streamline. For simplicity, we choose the streamline linking points C and E.

Close to point C, the speed of the rear interface is nil since it is pinned at the corners of the junction. Thus, the capillary drop at the receding interface is approximated as

$$\Delta P^{\text{r}}_{\text{cap}} = \gamma\left(\frac{1}{R^{\text{r}}} + \frac{2}{b}\right), \tag{20}$$

where R^{r} is the in-plane radius of the receding interface (see Fig. 11b) and is expressed as

$$R^{\text{r}} = \frac{w_{\text{o}}}{1 + \cos\theta^{\text{r}}}. \tag{21}$$

For the front interface, we assume that the speed of the contact line at point E establishes the contact angle θ^{a} and that θ^{a} is the same in the thickness and in the plane. Therefore, the capillary drop at the advancing interface reads

$$\Delta P^{\text{a}}_{\text{cap}} = \gamma\left(\frac{1}{R^{\text{a}}} - \frac{2\cos\theta^{\text{a}}}{b}\right), \tag{22}$$

where R^{a} is the in-plane radius of the advancing interface, calculated from geometry as

$$R^{\text{a}} = \frac{w_{\text{o}}}{1 - \cos\theta^{\text{a}}}. \tag{23}$$

The viscous term in Eq. (1) is approximated as a dissipation term in a Hele–Shaw geometry (since $b/w_{\text{o}} \simeq 0.18$), leading to

$$P_{\text{visc}} = \frac{12\eta}{b^2} L_{\text{m}} V_{\text{m}}, \tag{24}$$

where L_{m} is the length of the streamline C–E and V_{m} the mean speed of the fluid particles between points C and E. As stated above, the speed at point C is nil and the speed at point E is related to the contact angle by Tanner's law (Eq. (5)) as

$$V_{\text{E}} = \frac{\gamma}{\eta}\text{Ca}_{\text{E}} = \frac{\gamma(\theta^{\text{a}})^3}{6\eta\Gamma}. \tag{25}$$

We estimate the quantities V_{m} and L_{m} to first order as $V_{\text{m}} = (V_{\text{E}} + V_{\text{C}})/2$ and $L_{\text{m}} = y_{\text{E}} - w_{\text{i}}/2$, where $y_{\text{E}} = w_{\text{o}}/\tan(\theta^{\text{a}}/2)$ is the distance from point E to the centerline of the inlet channel (see Fig. 11b).

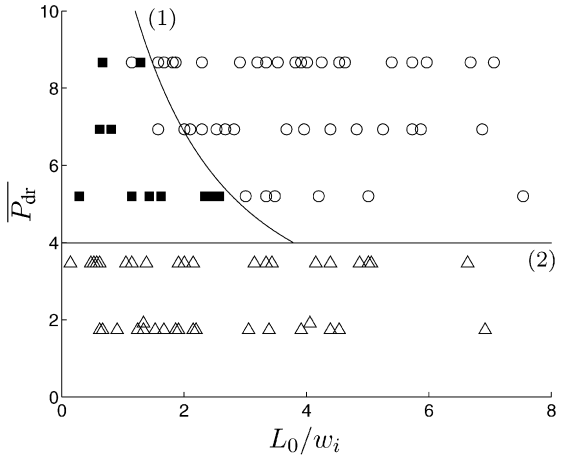

Fig. 12. Experimental $\overline{P_{\text{dr}}}$–L_0/w_{i} diagram and theoretical transitions. (1) Rupture-splitting transition corresponding to Eq. (27) with θ^{a} varying from $\pi/6$ to $\pi/3$ and $(6\Gamma)^{1/3} = 4.9$. (2) Threshold pressure (Eq. (14)).

Finally, combining the terms above leads to the pressure balance across the plug

$$P_{\text{dr}} \simeq \gamma\left[2\frac{y_{\text{E}} - w_{\text{i}}/2}{\Gamma b^2}\left(\theta^{\text{a}}\right)^3 + \frac{1}{R^{\text{a}}} + \frac{1}{R^{\text{r}}} + \frac{2}{b}\left(1 - \cos\theta^{\text{a}}\right)\right], \tag{26}$$

which accounts for the dynamic relation between θ^{a} and P_{dr}.

Using a reference pressure γ/w_{i} and expressing the different quantities as functions of θ^{a}, $w_{\text{i}}/w_{\text{o}}$, w_{o}/b and w_{i}/b, Eq. (26) reads in a nondimensional form

$$\begin{aligned}\overline{P_{\text{dr}}} \simeq{}& \left[2\frac{w_{\text{o}}}{b}\frac{w_{\text{i}}}{b}\left(\tan\frac{\theta^{\text{a}}}{2}\right)^{-1} - \left(\frac{w_{\text{i}}}{b}\right)^2\right]\frac{(\theta^{\text{a}})^3}{\Gamma} \\ &+ \left[1 + \cos\left(2\arctan\frac{w_{\text{i}}}{2w_{\text{o}}}\right)\right]\frac{w_{\text{i}}}{w_{\text{o}}} \\ &+ \left[\frac{2w_{\text{i}}}{b} + \frac{w_{\text{i}}}{w_{\text{o}}}\right]\left(1 - \cos\theta^{\text{a}}\right).\end{aligned} \tag{27}$$

5.2.3. Summary of the model

The geometrical condition provides a relation between L_{crit} and θ^{a} (Eq. (19)) while θ^{a} may be related to P_{dr} using the pressure balance of Eq. (26). For a given value of θ^{a}, we are now able to estimate the value of P_{dr} corresponding to L_{crit}. By varying θ^{a} from $\pi/6$ to $\pi/3$, we obtained the results plotted in their dimensionless form in Fig. 12, using $\Gamma = 20$ which is the value obtained from straight channel experiments. The quantitative and qualitative behaviors of the theoretical transition are in good agreement with the experimental data.

6. Conclusion

Our experiments on plug propagation in straight microchannels of rectangular cross section showed good agreement with previous studies in capillaries with circular sections [1], in spite of the large aspect ratio of our channels. In particular, the two principal radii of curvature could be used to account for the capillary effects at the advancing and receding interfaces and

effects of draining in the corners could be ignored for sufficiently fast propagation of the plugs.

Experiments through bifurcations show three distinct behavior regimes: blocking of the plugs at the bifurcation for small driving pressures, rupture and channel reopening, or splitting into two daughter plugs. The transitions between these three behaviors may be explained by invoking geometric constraints combined with capillary effects for the case of blocking, or a visco-capillary balance for the rupture vs splitting transition.

These results reproduce some of the known phenomenologies in pulmonary airway flows and geological flows, such as the existence of threshold pressures [10,14,15] or the different mechanisms of transport of a liquid bolus [16,17]. However, they benefit from having a well described geometry and direct access to the complete plug dynamics at all times. Combined with the advantages of microfluidic fabrication techniques, this study will lead to new experimental models of network dynamics, with implications in biofluid or porous media flows.

Acknowledgment

The authors acknowledge helpful discussions with José Bico and Matthias Heil.

References

[1] J. Bico, D. Quéré, J. Colloid Interface Sci. 243 (2001) 262–264.
[2] P.G. de Gennes, Rev. Mod. Phys. 57 (1985) 827–863.
[3] D. Halpern, O.E. Jensen, J.B. Grotberg, J. Appl. Physiol. 85 (1998) 333–352.
[4] R. Lenormand, C. Zarcone, SPE Proc. (1984) 13264.
[5] S.R. Quake, A. Scherer, Science 290 (2000) 1536–1540.
[6] H. Song, J.D. Tice, R.F. Ismagilov, Angew. Chem. Int. Ed. 42 (2003) 768–772.
[7] J.N. Lee, C. Park, G.M. Whitesides, Anal. Chem. 75 (2003) 6544–6554.
[8] P. Aussillous, D. Quéré, Phys. Fluids 12 (2000) 2367–2371.
[9] H.A. Stone, A.D. Stroock, A. Ajdari, Annu. Rev. Fluid Mech. 36 (2004) 381–411.
[10] R. Lenormand, J. Fluid Mech. 135 (1983) 337–353.
[11] R.L. Hoffman, J. Colloid Interface Sci. 50 (1975) 228–241.
[12] C. Treviño, C. Ferro-Fontán, F. Méndez, Phys. Rev. E 58 (1998) 4478–4484.
[13] F.P. Bretherton, J. Fluid Mech. 10 (1961) 166.
[14] A. Majumdar, A.M. Alencar, S.G. Buldyrev, Z. Hantos, Z.H. Stanley, B. Suki, Phys. Rev. E 67 (2003) 031912.
[15] B. Legait, C. R. Acad. Sci. Paris, Sér. II 292 (1981) 1111–1114.
[16] F.F. Espinosa, R.D. Kamm, J. Appl. Physiol. 86 (1999) 391–410.
[17] K.J. Cassidy, N. Gavriely, J.B. Grotberg, J. Biomech. Eng. 123 (2001) 580–590.